
Dislocation-ledge coupling drives non-conservative migration of semicoherent precipitate interfaces

Jin-Yu Zhang^{a,b,c}, Juan Du^{a,d}, Lin Yang^e, Frédéric Mompiou^d, Shigenobu Ogata^{b*},

Wen-Zheng Zhang^{a*}

^a Key Laboratory of Advanced Materials (MOE), School of Materials Science and Engineering, Tsinghua University, Beijing, 100084, China

^b Department of Mechanical Science and Bioengineering, The University of Osaka, Osaka, 560-8531, Japan

^c Department of Physics, McGill University, 3600 University Street, Montréal, Québec, H3A 2T8, Canada

^d CEMES-CNRS, Université de Toulouse, 29 rue J. Marvig, Toulouse, 31055, France

^e School of Materials Science and Engineering, Beijing Institute of Technology, Beijing, 100084, China

* Corresponding authors:

Shigenobu Ogata, Email address: ogata@me.es.osaka-u.ac.jp

Wen-Zheng Zhang, Email address: zhangwz@tsinghua.edu.cn

Abstract

Precipitate shape and size control the strength and stability of many structural alloys, yet the microscopic mechanism by which semicoherent precipitate interfaces migrate remains unclear. In particular, how dense interfacial dislocation networks move while accommodating transformation strain has resisted direct, time-resolved characterization. Here, we show that non-conservative motion of interfacial dislocations is intrinsically coupled to the nucleation and lateral propagation of nanoscale growth ledges, providing

a defect-based kinetic description of lath growth. Phase-field-crystal simulations of a prototypical face-centered cubic/body-centered cubic (FCC/BCC) transformation resolve strongly anisotropic interface kinetics: the end face advances continuously along the lath long axis, whereas facets thicken by discrete ledge sweeps accompanied by mixed glide–climb reactions in a closed dislocation network. Our crystallographic analyses predict the dislocation arrangements, rationalize the anisotropy via the geometry of misfit localization, and show how dislocation motion accommodates the transformation strain. In situ transmission electron microscopy of austenite precipitates in duplex stainless steel captures rapid ledge propagation on habit planes, consistent with the predicted migration mode. Our results bridge point-defect transport, dislocation reactions, and interface mobility, enabling quantitative, transferable predictions of precipitate morphology evolution.

Introduction

Precipitation strengthening underpins the performance of many structural alloys, where precipitate size, shape and spatial distribution set the strength–ductility balance and long-term microstructural stability^{1, 2}. In technologically important systems—including steels, Ti alloys, and Zr alloys—precipitates are commonly bounded by semicoherent interfaces: lattice misfit is accommodated by dense arrays and networks of interfacial dislocations³⁻¹⁰. Because these dislocations must move and reorganize as the interface advances, semicoherent interface migration is inherently defect-mediated and frequently produces highly anisotropic growth, such as rapid lengthening but slow thickening¹¹⁻¹³ that culminates in plate-, needle- or lath-like (Widmanstätten-type)

morphologies¹⁴⁻¹⁶.

Experiments have established that semicoherent interfaces around lath precipitates are structurally heterogeneous¹⁷⁻¹⁹. Many precipitates develop a long axis lying within dominant facets—typically a habit plane and one or more side facets^{3-6, 9, 20-22}—where misfit is accommodated by periodic arrays of interfacial dislocations. By contrast, end faces that are normal or inclined to the long axis often appear curved and exhibit more complex dislocation networks^{8, 23}. Nanoscale growth ledges²⁴⁻²⁶ have been reported on semicoherent interfaces across steels³, Ni/Cu-based alloys^{20, 27-29} and Ti/Zr alloys^{6, 9, 10, 16, 30-33}, and are widely invoked to rationalize stepwise facet advance. Experimental characterizations (including transmission electron microscopy (TEM)^{9, 29, 32} and high-resolution TEM^{3, 6, 33}) and crystallographic analyses^{34, 35} have resolved ledge character and associated dislocation content in several systems, yet direct time-resolved evidence capturing how ledges migrate while coupled to dense interfacial dislocation structures in three dimensions (3D) remains limited. Much of the experimental evidence is indirect—such as changes in ledge positions after short ageing treatments²⁰—with only a few *in situ* studies reporting lateral ledge motion on facets³⁴. Several works have further suggested that ledge-mediated migration may involve non-conservative defect processes^{6, 28, 34}, but how such processes operate at semicoherent precipitate interfaces, how they couple to interfacial dislocation motion, and how they accommodate transformation strain during sustained growth are still poorly understood.

Recent *in situ* atomic-resolution studies at grain boundaries have highlighted that non-conservative defect kinetics—through point-defect-assisted climb and

disconnection motion—can govern interface migration³⁶⁻⁴². Obtaining comparable mechanistic evidence at semicoherent precipitate interfaces is substantially more challenging because it requires adequate spatial resolution at elevated temperatures while the 3D precipitate geometry and crystallographically complex interfaces complicate interpretation. Dense interfacial dislocation arrays with nanometre-scale spacing can yield weak or overlapping contrast during dynamic migration, and free surfaces in TEM foils may bias defect behaviour relative to bulk conditions⁴³. These constraints motivate complementary approaches that can resolve the coupled evolution of interface structure, migration kinetics and precipitate morphology, while remaining quantitatively testable against experiments.

Atomistic simulations offer powerful mechanistic insight, yet most approaches are constrained either by time scales or by an incomplete treatment of diffusion and non-conservative defect motion. Molecular dynamics readily resolves conservative defect motion and interface migration coupled to dislocation glide⁴⁴⁻⁴⁸, but the accessible time scales and typical driving forces often emphasize shear-dominated responses rather than diffusive-time-scale growth^{49, 50}. Quasi-particle approaches, though beyond the spatiotemporal window of molecular dynamics, also simulate face-centered cubic/body-centered cubic (FCC/BCC) phase transformations mainly in a conservative manner^{51, 52}. Lattice-based Monte Carlo^{45, 53-57} approaches can access longer time scales and include diffusion, but commonly treat chemical degrees of freedom on lattice sites and may not naturally capture vacancy sources and sinks or the coupled evolution of explicit interfacial dislocation networks during sustained facet advance and ledge

propagation. Grand-canonical Monte Carlo can, in principle, enable open-ensemble exchange at interfaces and defects^{38, 58}, yet atom insertion and deletion remain energetically costly in crystalline structures, limiting efficient sampling of sustained facet advance and ledge propagation. Coarse-grained frameworks that evolve on diffusive time scales while retaining atomistic resolution of crystal symmetry—such as diffusive molecular dynamics⁵⁹ and phase-field-crystal (PFC) models^{60, 61} that have been applied to various microstructure evolution processes⁶²⁻⁶⁹—provide an attractive route to bridge this gap and to connect non-conservative defect kinetics to interface migration modes.

Here we establish a defect-based kinetic description of semicoherent precipitate growth by showing that non-conservative motion of interfacial dislocations is intrinsically coupled to the nucleation and lateral propagation of nanoscale growth ledges. We combine 3D PFC simulations with crystallographic O-lattice theory and *in situ* TEM to resolve precipitate growth through semicoherent interface migration in a prototypical FCC/BCC system. The simulations reveal strongly anisotropic growth kinetics: interfaces advance continuously along the lath long axis, whereas facet thickening proceeds intermittently via laterally propagating growth ledges. By tracking the time-resolved evolution of the interfacial defect structure in 3D, we show that interfacial dislocations on the habit plane, side facets and end faces connect into closed loops encircling the precipitate. These loops expand within well-defined loop planes that are generally not crystallographic slip planes, so their motion involves mixed glide-climb and requires point-defect transport. Crystallographic analyses predict the

arrangement of interfacial dislocation networks and explain how their non-conservative motion accommodates transformation strain and drives ledge-mediated facet kinetics, leading to a characteristic lath morphology. In situ TEM observations of austenite precipitates in duplex stainless steels capture rapid ledge propagation on habit planes and stepwise interface advance, consistent with the predicted migration mode. Together, these results bridge point-defect transport, dislocation reactions and interface kinetics, providing a quantitative and transferable framework for precipitate morphology evolution in defect-mediated phase transformations.

Results

PFC simulations of semicoherent precipitate growth

Starting from a spherical FCC nucleus embedded in a BCC matrix with a selected Kurdjumov-Sachs (K-S) orientation relationship variant, the precipitate rapidly evolves into a lath morphology bounded by broad habit planes, narrow side facets, and curved end faces (Fig. 1 and Supplementary Movie 1), with a long axis aligned with the parallel close-packed directions, $[0\bar{1}1]_f \parallel [1\bar{1}1]_b$. Both the habit planes and side facets remain semicoherent, accommodating misfit via periodic interfacial dislocation arrays with Burgers vectors of $\mathbf{b}_1 = [0\bar{1}1]_f/2|[1\bar{1}1]_b/2$ and $\mathbf{b}_2 = [10\bar{1}]_f/2|[11\bar{1}]_b/2$, respectively. At the end face, \mathbf{b}_1 and \mathbf{b}_2 segments intersect, and at some junctions, small segments of a third Burgers vector, $\mathbf{b}_3 = \mathbf{b}_1 + \mathbf{b}_2 = [1\bar{1}0]_f/2|[100]_b$, are present. The resulting key features, including lath shape with a long-axis, the two major facets, and interfacial dislocation structures (Burgers vectors, line directions, and dislocation

spacings), are in principle consistent with reports on lath austenite precipitates in duplex stainless steels⁵, and lath Cr precipitate in Cu-^{22, 29} and Ni-based alloys²⁸ (Table S1). Minor deviations from experiments mainly arise from the idealized lattice-parameter ratio ($a_f/a_b = \sqrt{3/2}$) adopted in the structural PFC model. This enforces an exact match between the Burgers-vector magnitudes and the close-packed plane spacings of the FCC and BCC lattices, respectively. In real alloys, small mismatches in these quantities can introduce slight angular deviations in the precipitate long axis and facet orientations, plus additional coarse-spaced misfit dislocations on side facets^{21, 27, 28}.

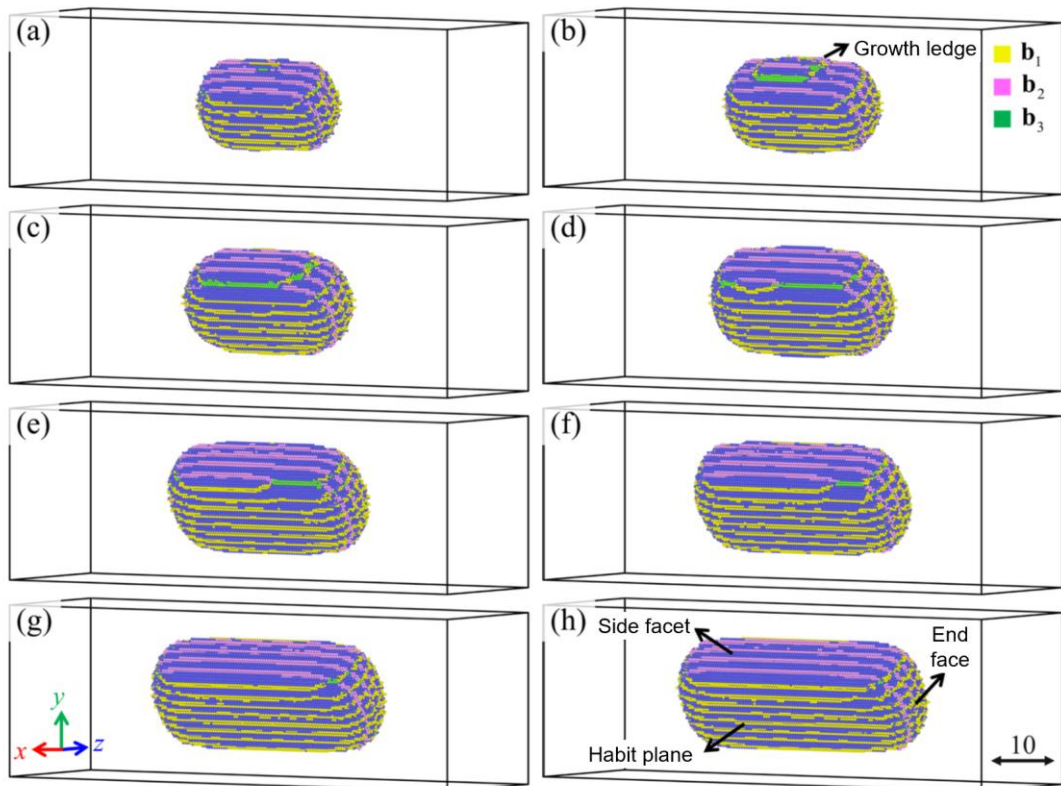


Fig. 1 Growth process of the FCC precipitate in the BCC matrix. **a** $t = 60$; **b** $t = 70$; **c** $t = 80$; **d** $t = 90$; **e** $t = 100$; **f** $t = 110$; **g** $t = 120$; **h** $t = 130$. Atoms belonging to the FCC phase are shown in blue. Atoms at the dislocation cores with different Burgers vectors are coloured distinctly (\mathbf{b}_1 , \mathbf{b}_2 , \mathbf{b}_3). Length and time are given in dimensionless units of the PFC model.

The lath morphology arises from strongly mode-dependent migration of the interfaces surrounding the precipitate. Despite carrying a dense dislocation network, the end face advances rapidly and continuously along the long axis. In contrast, the side facet migrates intermittently via a ledge mechanism (Supplementary Movie 2): a semicoherent ledge nucleates on a side facet and propagates laterally, accompanied by the formation/expansion of a \mathbf{b}_1 dislocation loop on the ledge risers. Ledge propagation is also highly anisotropic—nearly continuous parallel to the long axis but proceeding via kink nucleation and propagation in the transverse direction. Each ledge sweep translates the side facet and the \mathbf{b}_2 dislocation array by one ledge height; upon reaching facet edges, the ledge is incorporated into the habit plane and end face, widening the lath. The PFC-predicted ledge is consistent with the growth ledges reported on semicoherent FCC/BCC facets in multiple alloy systems, with a typical height of 1 nm²⁰,^{21, 27}.

Taken together, interfacial dislocations on the habit planes, side facets, and end faces connect into closed loops encircling the precipitate, consistent with previous interpretations of semicoherent precipitate interfaces^{8, 29, 70}. By tracking their time-resolved evolution, our simulations further show that these loops expand within well-defined loop planes that act as the effective shear planes for interfacial dislocation motion. Specifically, \mathbf{b}_1 dislocations on the habit planes and end faces close into loops whose loop plane is parallel to the side facet, whereas \mathbf{b}_2 dislocations on the side facets and end faces form loops parallel to the habit plane. Because the semicoherent facets in real materials are usually irrational, the loop planes are generally not typical slip planes,

so loop expansion often proceeds by mixed glide-climb motion and requires atomic diffusion. For example, the Burgers vector of \mathbf{b}_2 is inclined by $\sim 22^\circ$ relative to its loop plane, implying a climb component during advance. Consistently, Fig. S2 shows that during the ledge sweep across the side facet, \mathbf{b}_2 dislocations undergo non-conservative motion with a negative climb component, as expected when BCC transforms into the denser FCC structure. Overall, the simulation provides a 3D and time-resolved view that links non-conservative interfacial dislocation motion to facet/end-face migration modes and, ultimately, to the emergence of the Widmanstätten-type lath morphology widely observed in structural alloys.

In-situ TEM observations

To examine whether the growth-ledge-mediated advance inferred from simulations occurs on real FCC/BCC interfaces, we performed *in situ* TEM heating and tracked the habit plane migrations of freshly formed austenite precipitates in ferrite matrix, which exhibit long axes approximately aligned in the TEM foil (Fig. S3). The habit plane advanced in a mixed mode: discrete growth ledges traversed laterally along the long axis, while a concurrent, apparently ledge-free normal drift occurred within the experimental time resolution. In a representative event at 745 °C, three nanometre-scale growth ledges (noted 1, 2 and 3 in Fig. 2) were observed to migrate laterally over tens of seconds (Fig. 2a-d and Supplementary Movie 3), producing stepwise increments in the habit plane position. Ledges were identified by the discontinuity in the thickness fringes along the interface. Between ledge passages, the interface continued to migrate

forward normally, indicating an additional contribution to advance beyond resolvable ledge motion. Frame-difference images (Fig. 2e,f) isolate this behaviour and reveal a measurable net normal displacement accumulated during the intervals between successive ledge passages. Quantitatively, by averaging over the events shown in Fig. 2e,f, the lateral ledge-motion rate along the long axis is substantially higher than the averaged normal advance (~ 10 nm/s versus ~ 1.2 nm/s in this case), consistent with strongly direction-dependent kinetics of habit-plane migration and with the anisotropic ledge propagation resolved in the simulations.

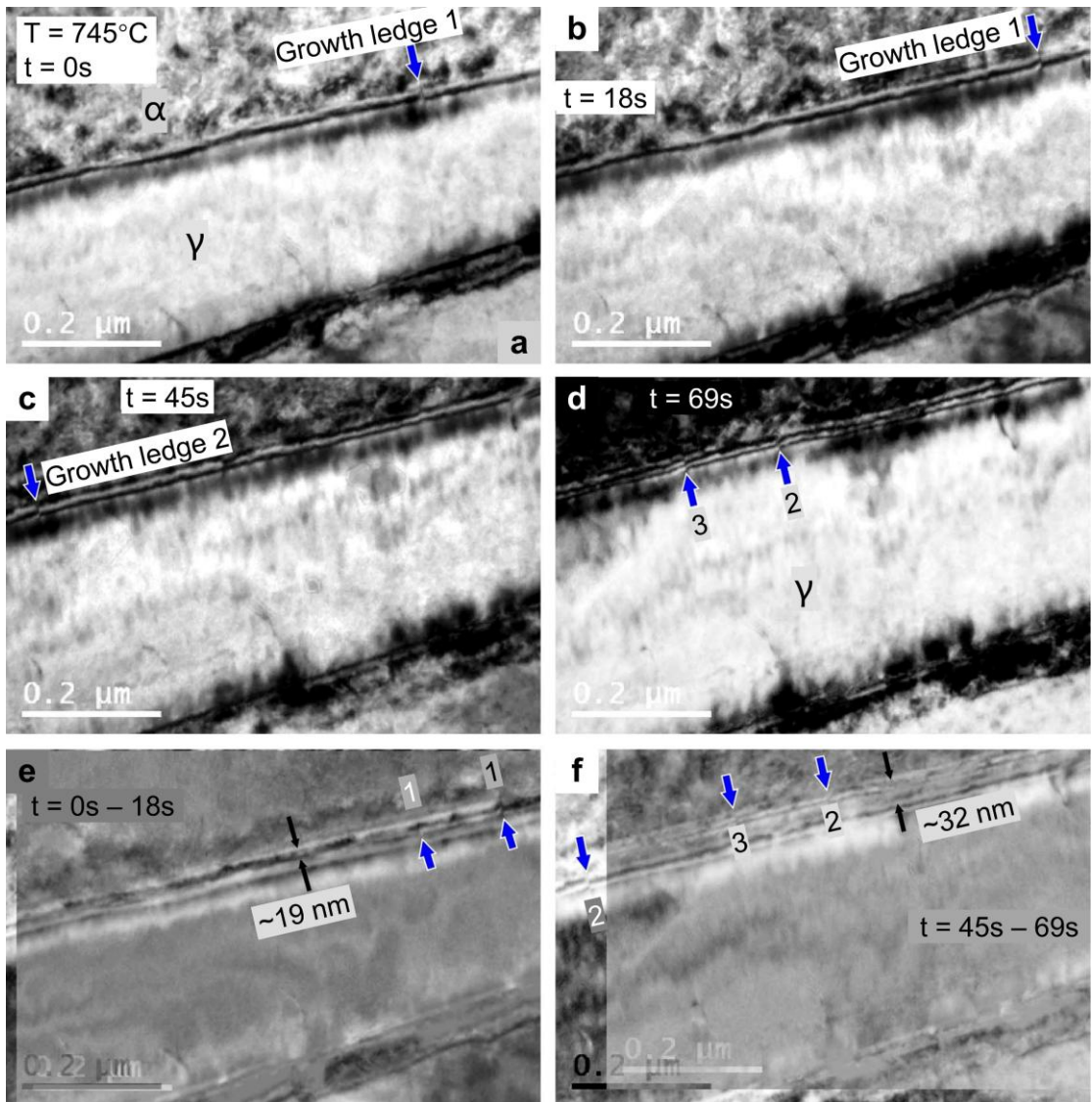


Fig. 2 Mixed-mode migration of an austenite/ferrite habit plane during in situ TEM heating. **a–d** Sequential frames at 745 °C showing three growth ledges (blue arrows) gliding laterally along the habit plane, approximately parallel to the long axis of the austenite precipitate. **e–f** Frame-difference images between **a**, **b**, and **c**, **d**, respectively, highlighting the net normal advance (black arrows) of the habit plane between ledge passages. Image displacements during the experiment are corrected using surface fiducial markers.

At a second habit plane captured at higher magnification (Fig. 3a–e and Supplementary Movie 4), the projected component of normal migration can be quantified more directly. Besides the lateral passage of discrete growth ledges, frame difference images reveal a fluctuating, ledge-free normal drift of the interface whose

magnitude varies from one time window (~ 0.1 nm/s, Fig. 3f) to another (~ 0.8 nm/s, Fig. 3g). Such fluctuations might result from transient pinning by local heterogeneities in the TEM foil. When a growth ledge is resolved (Fig. 3e), the corresponding difference image (49–63 s) reveals a clear spatial contrast in the normal advance (Fig. 3h): regions swept by the ledge have advanced by ~ 2 nm in projection, whereas adjacent regions not swept by the ledge have advanced by ~ 1 nm over the same time window. The difference (~ 1 nm) therefore provides an estimate of the ledge step height, superposed on a concurrent ledge-free normal drift. Together, these observations indicate that habit-plane advance comprises (i) growth-ledge-mediated, stepwise increments superposed on (ii) a concurrent normal drift that can proceed without a clearly resolvable ledge front at the current spatiotemporal resolution.

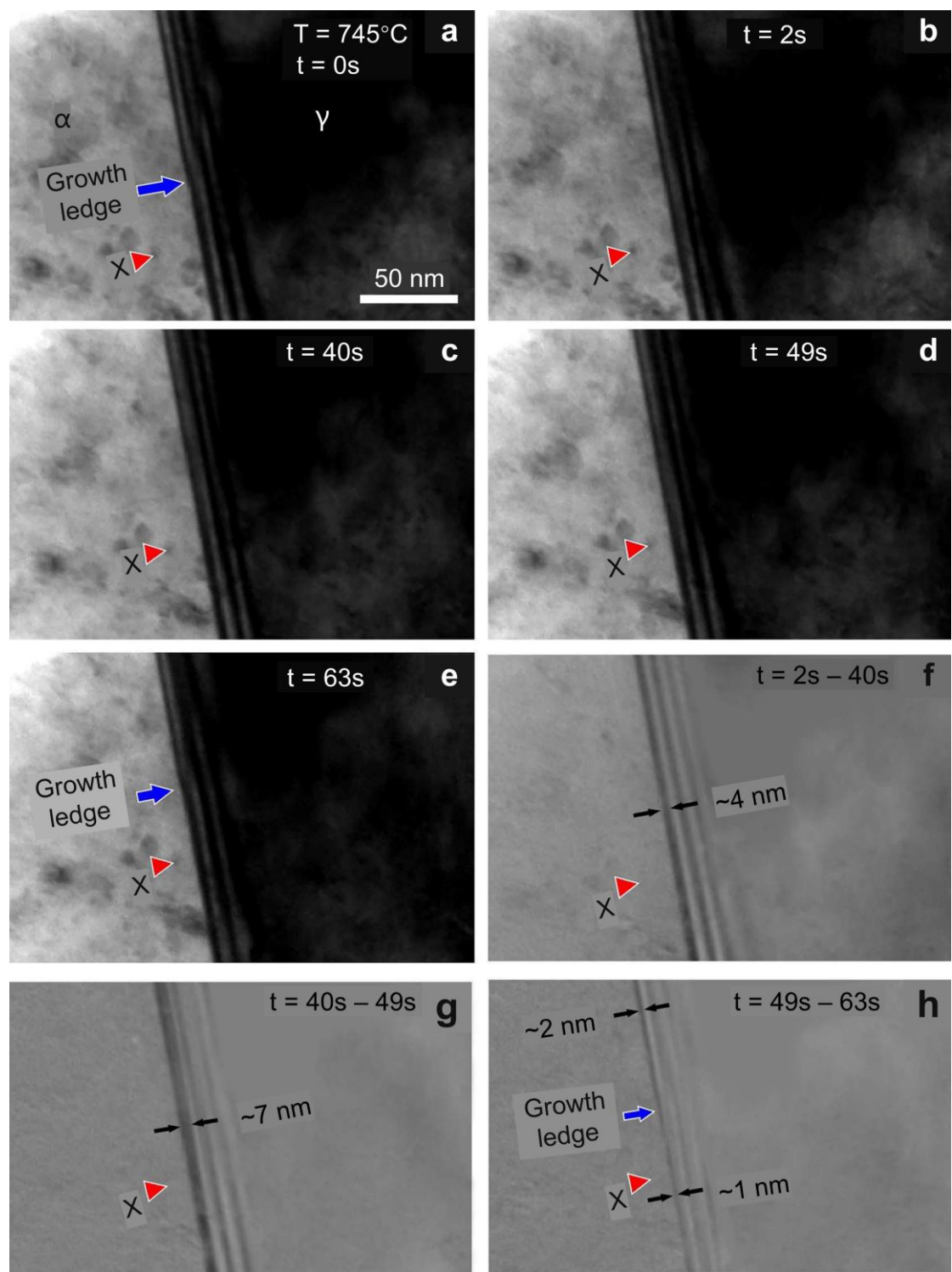


Fig. 3 Habit-plane advance resolved at higher magnification. **a–e** Sequential frames at $750\text{ }^{\circ}\text{C}$ showing the normal motion of an austenite/ferrite habit plane and lateral passage of a growth ledge (blue arrow). **f–g** Frame difference images for two ledge-free intervals, highlighting measurable normal displacements of the habit plane with different magnitudes. **h** Frame difference image for an interval containing a growth ledge passage, revealing an additional discrete normal increment associated with the ledge height.

Discussion

Interpretation of interfacial dislocations and anisotropic interface kinetics.

To rationalize the interfacial dislocation networks observed during PFC-simulated lath growth, we analysed the semicoherent FCC/BCC interfaces using O-lattice theory⁷¹. In the long-axis projection (Fig. 4a), edge-on O-lines (centres of coherent patches) and edge-on O-cell walls (loci of localized misfit) form an ordered pattern. Intersecting the O-cell walls with the habit plane and the side facets predicts periodic arrays of two dominant Burgers vectors, \mathbf{b}_1 and \mathbf{b}_2 , respectively, whereas intersection with the end face yields a dislocation network consisting of \mathbf{b}_1 , \mathbf{b}_2 , and short \mathbf{b}_3 segments. This predicted dislocation arrangement is in excellent agreement with the dislocation cores extracted from the PFC simulations (Fig. 4b,c), indicating that the simulated interfacial dislocation structure is largely determined by geometric lattice misfit across the habit plane, side facet, and end face. It is noted that in Fig. 4c, the \mathbf{b}_1 dislocation core appears invisible by a 2D Burgers circuit because of no in-plane Burgers vector component. Here, we identify \mathbf{b}_1 unambiguously via the 3D Nye-tensor analysis⁷². By contrast, the \mathbf{b}_2 dislocations retain a projected component ($[2\bar{1}\bar{1}]_f/4 | [2\bar{1}\bar{1}]_b/3$) and are readily characterized by Burgers-circuit closure failure. These atomic interface structures are consistent with prior high-resolution TEM observations along the parallel closed-packed directions (e.g., Fig. 6 of Ref. ²⁷).

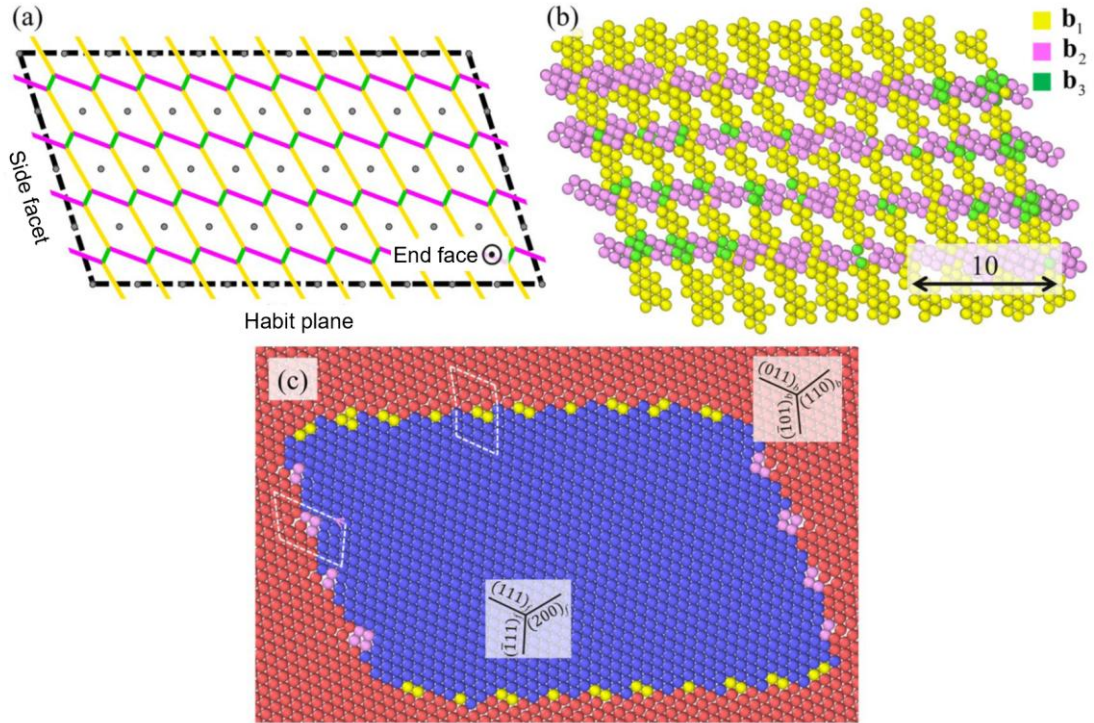


Fig 4. O-lattice prediction and PFC-resolved interfacial dislocations viewed along the long axis. **a** O-lattice construction viewed from the long axis: grey dots mark O-lines and coloured segments indicate O-cell walls associated with different Burgers vectors; dashed lines outline the traces of the habit plane and side facet, and the end-face region nearly normal to the long axis. **b** PFC snapshot showing the corresponding interfacial dislocation network. All the atoms inside the crystals are removed. **c** The cross-sectional view of the precipitate. Atoms in FCC and BCC are coloured blue and red, respectively.

Intersecting the O-cell walls with the full 3D precipitate interfaces predicts a closed, looped dislocation network in which segments on different interfaces connect across edges (Fig. 5b). During growth ledge nucleation and propagation, this network undergoes systematic dislocation reactions, in agreement with the PFC-resolved dynamics (Fig. 5 and Fig. S4). A pre-existing \mathbf{b}_2 segment on the side facet first splits into $-\mathbf{b}_1$ and \mathbf{b}_3 segments that decorate the two ledge risers with distinct orientations (Fig. 5b; Fig. S4b). As the riser merges back into the facet, the \mathbf{b}_3 segment further decomposes into \mathbf{b}_1 and \mathbf{b}_2 , restoring the dominant $\mathbf{b}_1/\mathbf{b}_2$ dislocation lines on the facet

(Fig. 5e; Fig. S4d). During ledge propagation (Fig. 5c–d), riser advance normal to the long axis proceeds through kink nucleation (e.g., BC segment in Fig. 5h), providing a kink-controlled mechanism for transverse ledge motion, whereas the kinks sweep rapidly along the long axis.

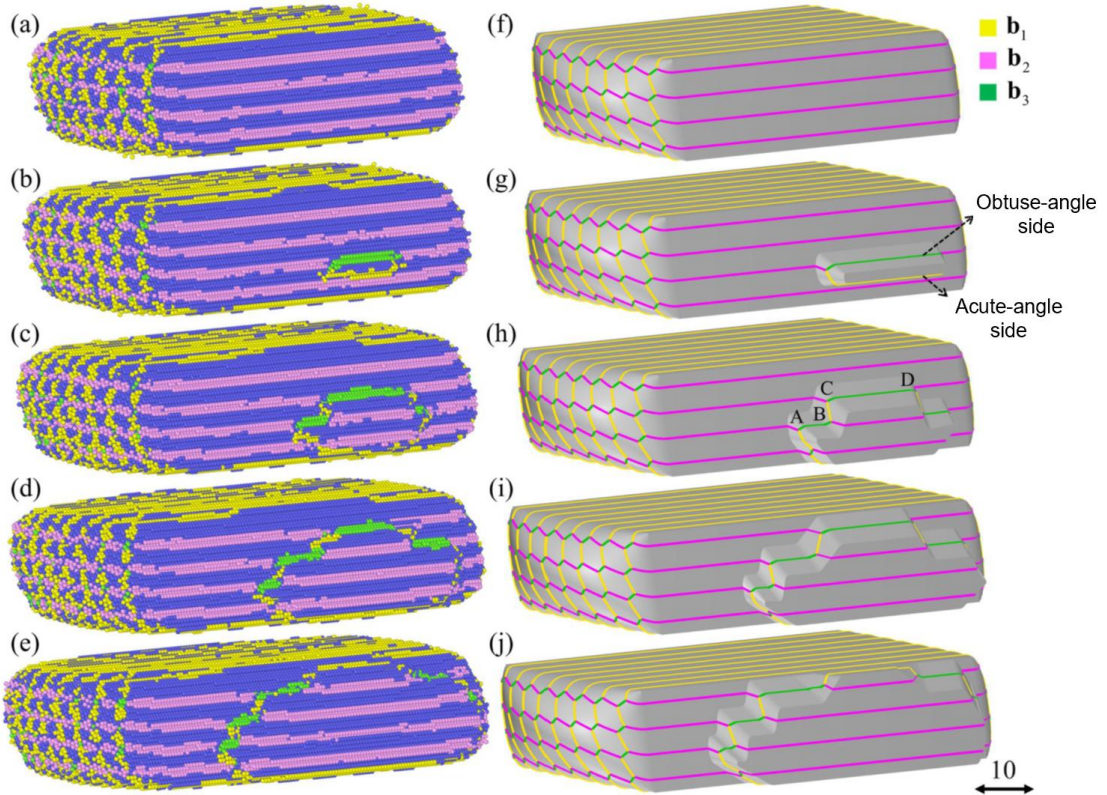


Fig 5. Growth ledge nucleation and propagation on a semicoherent side facet. a–e PFC snapshots showing the nucleation, lateral propagation, and annihilation of a growth ledge; f–j Corresponding 3D dislocation network calculated by the O-lattice theory, taking the interface geometry directly from the simulated precipitate. Dislocations are shown in different colours according to the Burgers vectors.

This O-lattice/O-cell-wall picture clarifies the origin of the strongly mode-dependent and anisotropic migration. Interfacial dislocations preferentially reside where the interface intersects the O-cell walls (Fig. 4a). Along the invariant (no-misfit) direction, i.e., the lath long axis, the O-cell walls form a continuous set of equivalent sites, so

dislocations on the end face and the kinks on the ledge riser can move continuously. In contrast, along the transverse direction (normal to the long axis), the dislocations are constrained to a discrete set of O-cell-wall intersection sites; departures from these sites generate long-range misfit strain, raising the elastic energy and hence the lattice resistance as discussed by Cahn⁷³. Compared with continuous motion of interfacial dislocation towards the direction (invariant line) that dislocations encountered almost no resistance force, growth-ledge formation on facets and kink formation on risers requires certain energy barriers, slowing transverse propagation. In this way, the lattice misfit distribution couples the 3D interfacial dislocation network to interface mobility, ultimately linking dislocation-level processes to the observed growth-ledge-mode migration and the emergence of the lath morphology. More broadly, this O-lattice-based geometric analysis of growth ledges is not restricted to the idealized lattice-parameter ratio used in the structural PFC model. It can be directly instantiated using experimental lattice parameters, enabling system-specific predictions of growth ledge structures and dislocation arrangements, as shown in our prior study³⁵. Additional illustrative comparisons with experimental growth ledge images and corresponding geometric constructions across multiple alloy systems are provided in Supplementary Materials.

Transformation strain accommodation by dislocation motion

Having established that the interfacial dislocation network is largely determined by lattice misfit and reorganizes through ledge/kink processes, we next ask what this collective motion accomplishes at the continuum level: specifically, how lath growth

accommodates the transformation strain without introducing extensive long-range plasticity in the surrounding matrix. To connect the interfacial dislocation dynamics in our simulations with the macroscopic transformation strain during lath growth, we adopt a displacement-field decomposition in which the transformation distortion is represented by shears of three independent dislocation sets⁷⁴⁻⁷⁶. In this framework, the transformation displacement matrix \mathbf{T} can be expressed as $\mathbf{T} = \mathbf{b}_{I\alpha}\Delta\mathbf{g}_I^T + \mathbf{b}_{II\alpha}\Delta\mathbf{g}_{II}^T + \mathbf{b}_{III\alpha}\Delta\mathbf{g}_{III}^T$ ⁷⁶, where the shear plane $\Delta\mathbf{g}_i^T = \mathbf{g}_{i\gamma}^T\mathbf{T} = \mathbf{g}_{i\gamma}^T - \mathbf{g}_{i\alpha}^T$ ($i = I, II, III$) is the difference between corresponding reciprocal vectors of the product (γ) and parent (α) lattices and $\mathbf{g}_{i\alpha}^T\mathbf{b}_{j\alpha} = \delta_{ij}$. For lath-shaped precipitates, the $\Delta\mathbf{g}_i$ vectors are known to be the normals of the observed facets^{4, 5, 9, 10, 18, 23}. In our PFC simulation geometry, under an idealized lattice parameter ratio, the transformation-strain accommodation is effectively dominated by two dislocation shears (\mathbf{b}_1 and \mathbf{b}_2) on the facets.

A key limitation of this classical decomposition is that it specifies the required shears kinematically, but does not reveal how they are dynamically realized during precipitate growth when the relevant “shear planes” are generally not crystallographic slip planes. Our time-resolved 3D simulations resolve this missing link. As the precipitate evolves, interfacial dislocations on the habit plane, side facets, and end faces connect into closed loops encircling the precipitate, and these loops expand within well-defined loop planes consistent with the $\Delta\mathbf{g}$ -defined shear-plane geometry. Because these semicoherent facets are typically irrational, the Burgers vectors are generally inclined with respect to the loop planes, so loop expansion proceeds by mixed glide-climb rather than purely conservative glide. This non-conservative character is directly observed during ledge-

mediated facet advance (Fig. S2), where interfacial dislocations acquire a negative climb component concurrent with interface migration, consistent with densification of the transforming α lattice into γ .

In real materials, such mixed glide-climb on semicoherent interfaces can be enabled by diffusion in a long-range from bulks or over interfacial (short-cut) length scales, with locally compensating positive/negative climb by different dislocations that reduce net point-defect transport⁷⁷. Overall, the displacement decomposition identifies the shears required for transformation-strain cancellation, whereas our simulations provide a 3D, time-resolved mechanism for how a closed interfacial dislocation network collectively delivers these shears during lath growth—thereby accommodating transformation strain without invoking long-range plasticity in the surrounding matrix.

Two typical interface migration modes

Two broad, conceptually useful distinctions have been emphasized in classic discussions of crystalline interface motions. Sutton and Balluffi⁷⁷ distinguished conservative versus non-conservative migration by whether long-range diffusion is required, whereas Cahn⁷³ emphasized that interface advance may occur either as normal motion or via lateral steps under different driving forces. A disconnection-based description has been proposed as a useful framework for interpreting grain-boundary kinetics across these viewpoints^{49, 78, 79}. These studies provide a useful vocabulary for organizing observations, but they do not, by themselves, specify the microscopic mechanism for 3D semicoherent FCC/BCC interfaces that contain complex interfacial

dislocation networks.

Recent atomistic simulations have clarified the conservative limit, in which interfaces advance rapidly through diffusion-free, largely glissile dislocation motion, producing an overall normal interface migration accompanied by macroscopic shear⁴⁴⁻⁴⁸. In this study, we revealed the complementary non-conservative limit within a single 3D and time-resolved precipitate growth process. Combining 3D PFC simulations with the O-lattice/O-cell construction, we directly resolve how a closed interfacial dislocation network reorganizes through growth ledge nucleation, propagation, and annihilation on semicoherent facets, thereby coupling atomic diffusion (point-defect level) and mixed glide-climb dislocation reactions (line-defect level) to growth-ledge-mediated facet migration (planar-defect level), and ultimately to the emergence of a lath-shaped precipitate whose transformation strain is accommodated (bulk level). When the driving force is sufficiently large to overcome the resistance force, continuous motion normal to the facet is possible, as typically occurs to martensitic phase transformations near-surface precipitations⁸⁰⁻⁸³. When the driving force is not large enough against the resistance force for continuous motion, nucleation and mixed motions of dislocations associated with ledges and kinks at ledges are an effective mode for the facets or the riser planes to advance.

At intermediate driving forces, a mixed mode combining growth-ledge mode and an apparently continuous normal drift can emerge. In situ TEM supports this crossover picture: discrete growth ledges traverse along the long-axis direction, while the interface also exhibits an apparently ledge-free normal drift whose rate fluctuates within

the current spatiotemporal resolution. The associated misfit strain of precipitate growth may be relaxed through the foil surface, making the continuous mode easier than in bulk. Moreover, our prior *in situ* TEM investigations of strain fields and plasticity around an advancing tip indicate that interfacial motion can locally generate dislocations toward the surface, which relax stresses in the surrounding matrix^{84, 85}. Together, the combined picture from prior molecular dynamics simulations (conservative limit), our 3D PFC/O-lattice analysis (non-conservative limit), and *in situ* TEM observations suggests that phase-transformation interfaces can be viewed through a point-line-planar-bulk hierarchy, where the availability of point-defect transport regulates whether interfacial dislocations move by glide alone or by mixed glide-climb, thereby selecting the operative planar migration mode and, ultimately, the evolving 3D precipitate morphology and associated macroscopic strain. This perspective motivates unified atomistic modelling strategies that can capture both limits and their crossover under a realistic driving force and resistance force in the future.

Methods

Phase-field-crystal model

We employed the structural PFC model developed by Greenwood et al.⁸⁶⁻⁸⁸ to simulate phase transformations in an FCC/BCC system. The state variable is the dimensionless atomic density field $n(\mathbf{r})$. The free-energy functional takes the form⁸⁶:

$$F = \int d\mathbf{r} (n(\mathbf{r})^2/2 - \eta n(\mathbf{r})^3/6 + \chi n(\mathbf{r})^4/12) - \int d\mathbf{r} \int d\mathbf{r}' n(\mathbf{r}) C_2(|\mathbf{r} - \mathbf{r}'|) n(\mathbf{r}')/2, \quad (1)$$

where the first term is a local Landau-type polynomial expansion around a uniform

reference state, and the second term introduces crystallographic order through the two-body correlation kernel $C_2(|\mathbf{r} - \mathbf{r}'|)$. Following Greenwood et al., C_2 was constructed in reciprocal space as an envelope of Gaussian peaks^{87, 88}:

$$C_2^i(k) = \exp(-\sigma^2/\sigma_{Mi}^2) \exp(-(k - k_i)^2/2\alpha_i^2), \quad (2)$$

where k_i , α_i , and σ_{Mi} control the peak position, width, and the dependence on the effective-temperature parameter σ , respectively. To stabilize the FCC phase with a dimensionless lattice parameter $a_f = \sqrt{3/2}$, two peaks were used at $k_1 = 2\sqrt{3}\pi/a_f$ and $k_2 = 4\pi/a_f$, corresponding to $\{111\}_f$ and $\{200\}_f$ plane families, respectively. Under this parameterization, the BCC lattice parameter satisfies $a_b = 2\sqrt{2}\pi/k_1 = 1$ because the first peak corresponds to $\{110\}_b$. The bulk free-energy densities of the FCC and BCC phases were evaluated as a function of the effective-temperature parameter σ following the method in a prior study⁸⁷ (Fig. S1), which identifies the phase-stability crossover used to select transformation conditions.

The density field $n(\mathbf{r})$ evolved according to conserved dynamics⁶⁰:

$$\partial n(\mathbf{r})/\partial t = \nabla^2[\delta F/\delta n(\mathbf{r})] + \xi, \quad (3)$$

where ξ represents a colored Gaussian noise term. This equation conserves the spatial integral of $n(\mathbf{r})$ and enables evolutions on diffusive timescales within the PFC framework. Time integration was performed in reciprocal space using a semi-implicit Fourier-spectral scheme. We emphasize that the structural PFC simulations are used here to elucidate the coupled dislocation-ledge mechanism and the geometry-governed interface dynamics, rather than to quantitatively calibrate the dimensionless PFC time to experimental absolute time scales.

Initialization and analysis workflow

The initial configuration consisted of a spherical FCC precipitate embedded in a BCC matrix, with a dimensionless radius of 10 to suppress capillarity-driven shrinkage. The initial orientation relationship was set to the K-S orientation relationship with the variant $[0\bar{1}1]_f \parallel [1\bar{1}1]_b$ and $(111)_f \parallel (011)_b$. By adopting idealized lattice parameters ($a_f = \sqrt{3/2}a_b$), $[111]_f$ and $[011]_b$ have identical lengths, and they define the direction of the invariant-line. In addition, $(111)_f \parallel (011)_b$ define the direction of the invariant-line in reciprocal space. Therefore, three sets of O-lines are solvable for this special case, which simplifies the dislocation structures while retaining the key process of dislocation-mediated ledge mechanism of growth.

After simulation, atomic positions were extracted from the local maxima (density peaks) of $n(\mathbf{r})$. Local crystal structures (FCC/BCC/other) were identified using polyhedral template matching (PTM)⁸⁹ as implemented in OVITO⁹⁰. Interfacial dislocations were characterized by their spatial distribution and Burgers vectors, determined from the Nye tensor field evaluated on the extracted atomic configuration. The Nye tensor was computed and decomposed using singular value decomposition to obtain the dominant Burgers-vector content⁷².

In situ TEM experiments

A commercial duplex stainless steel with nominal composition Fe-24.9Cr-7.0Ni-3.1Mo (wt%) was used. For in situ observations of freshly nucleated austenite, 10×10

$\times 10$ mm³ blocks were encapsulated in evacuated silica tubes and solution-treated at 1300 °C for 30 min, followed by water quenching. TEM foils were prepared from 0.5-mm-thick slices by mechanical thinning and twin-jet electropolishing (Struers Tenupol-3) using 8 vol% perchloric acid in ethanol at 20 V and –30 °C. Immediately before heating experiments, foils were plasma cleaned (Solarus, Gatan; 1 min) to remove hydrocarbon contamination. In situ heating was conducted in a Philips CM20FEG microscope operated at 200 kV using a Gatan double-tilt heating holder. Samples were first heated to 700 °C at the maximum heating rate (~50 °C/min), then heated in 5 °C increments until interface migration or new austenite growth was observed (typically 720–850 °C). Videos were recorded using a Gatan Orius side-entry CCD camera at 15–24 fps, and key frames were extracted for subsequent analysis.

Crystallographic calculation of interfacial dislocations

Interfacial dislocation structures were determined corresponding to the locations of maximal misfit. The O-lattice theory⁷¹ provides a general tool for analysing misfit distribution in any interface. For the K-S orientation relationship considered here, using the special lattice parameter ratio, the misfit at any interface can be accommodated by interfacial dislocations whose Burgers vectors lie within the parallel planes (111)_f || (011)_b, namely, $\mathbf{b}_1 = [0\bar{1}1]_f/2|[1\bar{1}1]_b/2$, $\mathbf{b}_2 = [10\bar{1}]_f/2|[11\bar{1}]_b/2$, and $\mathbf{b}_3 = [1\bar{1}0]_f/2|[100]_b$, where symbol “|” denotes corresponding vectors across the transformation. The position of an O-lattice element (position of zero misfit) is defined by a vector, \mathbf{x}^0 , solved from: $\mathbf{T}\mathbf{x}^0 = \sum_i k_i \mathbf{b}_{i\alpha}$ ⁷¹, where k_i are integers, $\sum_i k_i \mathbf{b}_{i\alpha}$

indicates any the translational vectors in α phase. $\mathbf{T} = \mathbf{I} - \mathbf{A}^{-1}$ is the displacement matrix that links a position \mathbf{x}_γ with its associated displacement $\mathbf{x}_\gamma - \mathbf{x}_\alpha$, which are related by $\mathbf{x}_\gamma = \mathbf{A}\mathbf{x}_\alpha$. Here, \mathbf{A} represents the deformation matrix transforming α lattice to γ lattice. A set of O-cell walls between O-elements corresponds to positions of maximal misfit, are defined by a reciprocal vector, \mathbf{c}^0 , related to a Burgers vector, $\mathbf{b}_{i\alpha}$, by $\mathbf{c}^0 = \mathbf{T}^T \mathbf{b}_{i\alpha} / |\mathbf{b}_{i\alpha}|^{291}$. The dislocations are defined by the intersections between the O-cell walls and an interface, and the Burgers vector of the dislocations is $\mathbf{b}_{i\alpha}$ associated with the particular set of O-cell walls. The interfacial dislocations determined based on the O-lattice theory were employed to compare with PFC-predicted defect structures and experimental observations.

Data availability

The data that support the findings of this study are available within the Article and its Supplementary Information. Additional data are available from the corresponding author upon reasonable request.

Code availability

The scripts used for data analysis and visualization are available from the corresponding author upon reasonable request.

References

1. Brown LM, Ham RK. Dislocation-particle interactions. In: *Strengthening methods in crystals* (eds Kelly A, Nicholson RB). Elsevier (1971).

- 2. Ardell AJ. Precipitation hardening. *Metall. Trans. A* **16**, 2131-2165 (1985).
- 3. Jiao HS, Aindow M, Pond RC. Precipitate orientation relationships and interfacial structures in duplex stainless steel Zeron-100. *Phil. Mag.* **83**, 1867-1887 (2003).
- 4. Qiu D, Zhang W-Z. A TEM study of the crystallography of austenite precipitates in a duplex stainless steel. *Acta Mater.* **55**, 6754-6764 (2007).
- 5. Du J, Mompiou F, Zhang W-Z. A TEM study of the crystallography of lath-shaped austenite precipitates in a duplex stainless steel. *J. Mater. Sci.* **52**, 11688-11700 (2017).
- 6. Furuhara T, Ogawa T, Maki T. Atomic-structure of interphase boundary of an α -precipitate plate in a β Ti-Cr Alloy. *Phil. Mag. Lett.* **72**, 175-183 (1995).
- 7. Zheng YF, Williams REA, Viswanathan GB, Clark WAT, Fraser HL. Determination of the structure of α - β interfaces in metastable β -Ti alloys. *Acta Mater.* **150**, 25-39 (2018).
- 8. Zhang Y-S, Zhang J-Y, Zhang W-Z. Dislocation network on the curved end face of α precipitates in a Ti-8 wt.% Fe alloy. *Phil. Mag.* **102**, 1-14 (2021).
- 9. Zhang W-Z, Perovic V, Perovic A, Weatherly GC, Purdy GR. The structure of HCP-BCC interfaces in a Zr-Nb alloy. *Acta Mater.* **46**, 3443-3453 (1998).
- 10. Zhang W-Z, Purdy GR. A TEM study of the crystallography and interphase boundary structure of α precipitates in a Zr-2.5wt%Nb alloy. *Acta Metall. Mater.* **41**, 543-551 (1993).
- 11. Kinsman KR, Eichen E, Aaronson HI. Thickening kinetics of proeutectoid ferrite plates in Fe-C alloys. *Metall. Trans. A* **6**, 303 (1975).
- 12. Phelan D, Stanford N, Dippenaar R. In situ observations of Widmanstätten ferrite formation in a low-carbon steel. *Mater. Sci. Eng. A* **407**, 127-134 (2005).
- 13. Phelan D, Reid M, Stanford N, Dippenaar R. In-situ observations of phase transformations in titanium. *JOM* **58**, 67-69 (2006).
- 14. Ohmori Y, Ohtsubo H, Jung YC, Okaguchi S, Ohtani H. Morphology of bainite and widmanstätten ferrite. *Metall. Mater. Trans. A* **25**, 1981-1989 (1994).
- 15. Banerjee D, Williams JC. Perspectives on titanium science and technology. *Acta Mater.* **61**, 844-879 (2013).
- 16. Banerjee S, Dey GK, Srivastava D, Ranganathan S. Plate-shaped transformation products in zirconium-base alloys. *Metall. Mater. Trans. A* **28**, 2201-2216 (1997).
- 17. Zhang MX, Kelly PM. Crystallographic features of phase transformations in solids. *Prog. Mater. Sci.* **54**, 1101-1170 (2009).
- 18. Zhang W-Z, Weatherly GC. On the crystallography of precipitation. *Prog. Mater. Sci.* **50**, 181-292 (2005).
- 19. Howe JM, Pond RC, Hirth JP. The role of disconnections in phase transformations. *Prog. Mater. Sci.* **54**, 792-838 (2009).
- 20. Chen G, Spanos G, Masumura RA, Reynolds WT. Effects of ledge density on the morphology and growth kinetics of precipitates in a Ni-Cr Alloy. *Acta Mater.* **53**, 895-906 (2005).
- 21. Luo CP, Weatherly GC. The interphase boundary structure of precipitates in a

Ni-Cr alloy. *Phil. Mag. A* **58**, 445-462 (1988).

- 22. Luo CP, Dahmen U, Westmacott KH. Morphology and crystallography of Cr precipitates in a Cu-0.33 wt% Cr alloy. *Acta Metall. Mater.* **42**, 1923-1932 (1994).
- 23. Ye F, Zhang W-Z. Dislocation structure of non-habit plane of α precipitates in a Ti-7.26 wt.% Cr alloy. *Acta Mater.* **54**, 871-879 (2006).
- 24. Aaronson HI. Decomposition of austenite by diffusional process. In: *Interscience* (eds Zackay VF, Aaronson HI) (1962).
- 25. Weatherly GC. The structure of ledges at plate-shaped precipitates. *Acta Metall.* **19**, 181-192 (1971).
- 26. Shiflet GJ, Mangan MA, Meng WG. Growth by Ledges. *Interface Sci.* **6**, 133-154 (1998).
- 27. Furuhara T, Wada K, Maki T. Atomic-structure of interphase boundary enclosing BCC precipitate formed in FCC matrix in a Ni-Cr alloy. *Metall. Mater. Trans. A* **26**, 1971-1978 (1995).
- 28. Chen JK, Chen G, Reynolds WT. Interfacial structure and growth mechanisms of lath-shaped precipitates in Ni-45 wt% Cr. *Phil. Mag. A* **78**, 405-422 (1998).
- 29. Luo CP, Dahmen U. Interface structure of faceted lath-shaped Cr precipitates in a Cu-0.33 wt% Cr alloy. *Acta Mater.* **46**, 2063-2081 (1998).
- 30. Menon ESK, Aaronson HI. Interfacial structure of Widmanstatten plates in a Ti-Cr alloy. *Acta Metall.* **34**, 1975-1981 (1986).
- 31. Furuhara T, Lee HJ, Menon ESK, Aaronson HI. Interphase boundary structures associated with diffusional phase-transformations in Ti-base alloys. *Metall. Trans. A* **21**, 1627-1643 (1990).
- 32. Furuhara T, Howe JM, Aaronson HI. Interphase boundary structures of intragranular proeutectoid α plates in a hypoeutectoid Ti-Cr alloy. *Acta Metall. Mater.* **39**, 2873-2886 (1991).
- 33. Mills MJ, Hou DH, Suri S, Viswanathan GB. Orientation relationship and structure of α/β interfaces in conventional titanium alloys. In: *Boundaries & Interfaces in Materials: the David A. Smith Symposium* (1998).
- 34. Zhang J-Y, Zhang Y-S, Mompiou F, Zhang W-Z. Structures and migrations of interfaces between β precipitates and α' matrix in a Ti-2.6 wt% Mo alloy. *Acta Mater.* **281**, 120429 (2024).
- 35. Zhang J-Y, Gao Y, Wang Y, Zhang W-Z. A generalized O-element approach for analyzing interface structures. *Acta Mater.* **165**, 508-519 (2019).
- 36. Wang L, *et al.* Tracking the sliding of grain boundaries at the atomic scale. *Science* **375**, 1261-1265 (2022).
- 37. Guo Y, *et al.* In situ observation of atomic-scale processes accomplishing grain rotation at mixed grain boundaries. *Acta Mater.* **241**, 118386 (2022).
- 38. Chu S, *et al.* In situ atomic-scale observation of dislocation climb and grain boundary evolution in nanostructured metal. *Nat. Commun.* **13**, 4151 (2022).
- 39. Tian Y, *et al.* Grain rotation mechanisms in nanocrystalline materials: Multiscale observations in Pt thin films. *Science* **386**, 49-54 (2024).
- 40. Wang Z, *et al.* In situ atomic-scale observation of diffusion-assisted pure sliding

of coherent twin boundary in Pt. *Acta Mater.* **295**, 121188 (2025).

- 41. Li X, Cao G, Chen Y, Yue P, Song K, Wang J. Dislocation climb mediated Coble-type grain boundary deformation in gold nanocrystals. *Mater. Res. Lett.* **13**, 60-66 (2025).
- 42. Wei J, Feng B, Tochigi E, Shibata N, Ikuhara Y. Direct imaging of the disconnection climb mediated point defects absorption by a grain boundary. *Nat. Commun.* **13**, 1455 (2022).
- 43. Legros M, Mompiou F, Caillard D. Observing deformation in situ. *Nat. Mater.* **23**, 20-22 (2024).
- 44. Sun Z-P, Dai F-Z, Xu B, Zhang W-Z. Dislocation-mediated migration of interphase boundaries. *J. Mater. Sci. Technol.* **35**, 2714-2726 (2019).
- 45. Zhang J-Y, *et al.* Dislocation-mediated migration of the α/β interfaces in titanium. *Acta Mater.* **261**, 119364 (2023).
- 46. Zhang J-Y, Sun Z-P, Zhang Y-S, Zhang W-Z. Interface dislocation trajectory and long-range strain associated with the migration of semicoherent interfaces. *Acta Mater.* **277**, 120167 (2024).
- 47. Wang S, Wen T, Han J, Srolovitz DJ. Coherent and semicoherent α/β interfaces in titanium: structure, thermodynamics, migration. *npj Comput. Mater.* **9**, 216 (2023).
- 48. Maresca F, Curtin WA. The austenite/lath martensite interface in steels: Structure, athermal motion, and in-situ transformation strain revealed by simulation and theory. *Acta Mater.* **134**, 302-323 (2017).
- 49. Thomas SL, Chen K, Han J, Purohit PK, Srolovitz DJ. Reconciling grain growth and shear-coupled grain boundary migration. *Nat. Commun.* **8**, 1764 (2017).
- 50. Rohrer GS, *et al.* Grain boundary migration in polycrystals. *Annual Review of Materials Research* **53**, 347-369 (2023).
- 51. Borges Y, Zapolsky H, Ledue D, Patte R, Demange G. An atomistic model for the fcc \rightarrow bcc transformation in iron with the Nishiyama–Wasserman orientation relationship: Insight from the Quasi-particle Approach. *Acta Mater.* **297**, 121355 (2025).
- 52. Demange G, *et al.* Atomistic study of the fcc \rightarrow bcc transformation in a binary system: Insights from the Quasi-particle Approach. *Acta Mater.* **226**, 117599 (2022).
- 53. Liao H, Kimizuka H, Ishii A, Du J-P, Ogata S. Nucleation kinetics of the β'' precipitate in dilute Mg–Y alloys: A kinetic Monte Carlo study. *Scr. Mat.* **210**, 114480 (2022).
- 54. Liao H, Du J-P, Kimizuka H, Ogata S. Atomistic simulation of Guinier–Preston zone nucleation kinetics in Al–Cu alloys: A neural network-driven kinetic Monte Carlo approach. *Comput. Mater. Sci.* **251**, 113771 (2025).
- 55. Soisson F, Fu C-C. Cu-precipitation kinetics in α -Fe from atomistic simulations: Vacancy-trapping effects and Cu-cluster mobility. *Phys. Rev. B* **76**, 214102 (2007).
- 56. Clouet E, Nastar M, Sigli C. Nucleation of Al_3Zr and Al_3Sc in aluminum alloys: From kinetic Monte Carlo simulations to classical theory. *Phys. Rev. B* **69**,

064109 (2004).

- 57. Dai F-Z, Sun Z-P, Zhang W-Z. From coherent to semicoherent—Evolution of precipitation crystallography in an fcc/bcc system. *Acta Mater.* **186**, 124-132 (2020).
- 58. Vamvakopoulos E, Tanguy D. Equilibrium vacancy concentrations in $\Sigma=33(554)[1\bar{1}0]$ by grand canonical Monte Carlo simulations. *Phys. Rev. B* **79**, 094116 (2009).
- 59. Li J, Sarkar S, Cox WT, Lenosky TJ, Bitzek E, Wang Y. Diffusive molecular dynamics and its application to nanoindentation and sintering. *Phys. Rev. B* **84**, 054103 (2011).
- 60. Provatas N, Elder K. *Phase-field methods in materials science and engineering*. Wiley-VCH (2010).
- 61. Elder KR, Katakowski M, Haataja M, Grant M. Modeling elasticity in crystal growth. *Phys. Rev. Lett.* **88**, 245701 (2002).
- 62. Dontsova E, Rottler J, Sinclair CW. Solute-defect interactions in Al-Mg alloys from diffusive variational Gaussian calculations. *Phys. Rev. B* **90**, 174102 (2014).
- 63. Mamaev A, Provatas N. Phase-field crystal modeling of lamellar precipitation reactions. *Acta Mater.*, 121978 (2026).
- 64. Qiu C, *et al.* Grain boundaries are Brownian ratchets. *Science* **385**, 980-985 (2024).
- 65. Mendez JP, Ponga M. MXE: A package for simulating long-term diffusive mass transport phenomena in nanoscale systems. *Comput. Phys. Commun.* **260**, 107315 (2021).
- 66. Huang Y, Wang J, Wang Z, Li J. Atomic structures and migration mechanisms of interphase boundaries during body- to face-centered cubic phase transformations. *J. Appl. Cryst.* **52**, 1176-1188 (2019).
- 67. Yang T, *et al.* Non-conservative dynamics of lattice sites near a migrating interface in a diffusional phase transformation. *Acta Mater.* **127**, 481-490 (2017).
- 68. Berry J, Provatas N, Rottler J, Sinclair CW. Phase field crystal modeling as a unified atomistic approach to defect dynamics. *Phys. Rev. B* **89**, 214117 (2014).
- 69. Fallah V, Korinek A, Ofori-Opoku N, Provatas N, Esmaeili S. Atomistic investigation of clustering phenomenon in the Al–Cu system: Three-dimensional phase-field crystal simulation and HRTEM/HRSTEM characterization. *Acta Mater.* **61**, 6372-6386 (2013).
- 70. Forwood CT, Clarebrough LM. The dislocation structure of f.c.c.—b.c.c. interfaces in a Cu—Fe alloy. *Philosophical Magazine B* **59**, 637-665 (1989).
- 71. Bollmann W. *Crystal defects and crystalline interfaces*. Springer-Verlag (1970).
- 72. Dai F-Z, Zhang W-Z. An automatic and simple method for specifying dislocation features in atomistic simulations. *Comput. Phys. Commun.* **188**, 103-109 (2015).
- 73. Cahn JW. Theory of crystal growth and interface motion in crystalline materials. *Acta Metall.* **8**, 554-562 (1960).

- 74. Bollmann W. *Crystal lattices, interfaces, matrices*. Bollmann W (1982).
- 75. Knowles KM. The dislocation geometry of interphase boundaries. *Phil. Mag. A* **46**, 951-969 (1982).
- 76. Zhang W-Z. Decomposition of the transformation displacement field. *Phil. Mag. A* **78**, 913-933 (1998).
- 77. Sutton AP, Balluffi RW. *Interfaces in crystalline materials*. Oxford University Press (1995).
- 78. Han J, Thomas SL, Srolovitz DJ. Grain-boundary kinetics: A unified approach. *Prog. Mater. Sci.* **98**, 386-476 (2018).
- 79. Wei C, Thomas SL, Han J, Srolovitz DJ, Xiang Y. A Continuum Multi-Disconnection-Mode model for grain boundary migration. *J. Mech. Phys. Solids* **133**, 103731 (2019).
- 80. Qiu D, Zhang M-X, Kelly PM, Furuhara T. Crystallography of surface precipitates associated with shape change in a Ti-5.26 wt.% Cr alloy. *Acta Mater.* **61**, 7624-7638 (2013).
- 81. Watson JD, McDougall PG. The crystallography of widmanstätten ferrite. *Acta Metall.* **21**, 961-973 (1973).
- 82. Furuhara T, Ogawa T, Maki T. Surface relief effect and atomic site correspondence in the grain boundary α precipitation in a β Ti-Cr alloy. *Scr. Mat.* **34**, 381-386 (1996).
- 83. Lee HJ, Aaronson HI. Surface relief effects associated with proeutectoid α plates in a Ti-7.15 wt% Cr alloy. *Acta Metall.* **36**, 787-794 (1988).
- 84. Du J, Mompiou F, Zhang W-Z. In-situ TEM study of dislocation emission associated with austenite growth. *Scr. Mat.* **145**, 62-66 (2018).
- 85. Hirth JP, Pond RC. Compatibility and accommodation in displacive phase transformations. *Prog. Mater. Sci.* **56**, 586-636 (2011).
- 86. Greenwood M, Rottler J, Provatas N. Phase-field-crystal methodology for modeling of structural transformations. *Phys. Rev. E* **83**, 031601 (2011).
- 87. Greenwood M, Ofori-Opoku N, Rottler J, Provatas N. Modeling structural transformations in binary alloys with phase field crystals. *Phys. Rev. B* **84**, 064104 (2011).
- 88. Greenwood M, Provatas N, Rottler J. Free energy functionals for efficient phase field crystal modeling of structural phase transformations. *Phys. Rev. Lett.* **105**, 045702 (2010).
- 89. Larsen PM, Schmidt S, Schiøtz J. Robust structural identification via polyhedral template matching. *Model. Simul. Mater. Sci. Eng.* **24**, 055007 (2016).
- 90. Stukowski A. Visualization and analysis of atomistic simulation data with OVITO-the Open Visualization Tool. *Model. Simul. Mater. Sci. Eng.* **18**, 015012 (2010).
- 91. Zhang W-Z, Purdy GR. O-lattice analyses of interfacial misfit. I. General considerations. *Phil. Mag. A* **68**, 279-290 (1993).

Acknowledgements

J-Y.Z. would like to thank Prof. Nikolas Provatas and Dr. Nana Ofori-Opoku at McGill University for teaching the basic usage of structural PFC codes, and Dr. Rui-Xun Xie for technical assistance in setting up the GPU server used for running PFC simulations. J-Y.Z. and S.O. acknowledge the funding by projects of JSPS KAKENHI (Grant No. JP23K20037). W-Z.Z. acknowledges the supports from the National Natural Science Foundation of China (Grant No. 51871131) and the National Key Research and Development Program of China (Grant No. 2016YFB0701304). J-Y.Z. and J.D. acknowledge the China Scholarship Council (No. 201906210309 and No. 201506210313) for funding the stay at McGill University (Canada) and CEMES (France), respectively.

Author contributions

J-Y.Z. performed simulations and theoretical analyses and wrote the manuscript. J.D. carried out the experiments and analysed the data. L.Y. provided guidance on simulation work. F.M., S.O., and W.-Z.Z. contributed to the interpretation of the results and revised the manuscript.

Competing interests

The authors declare no competing interests.

Supplementary Materials

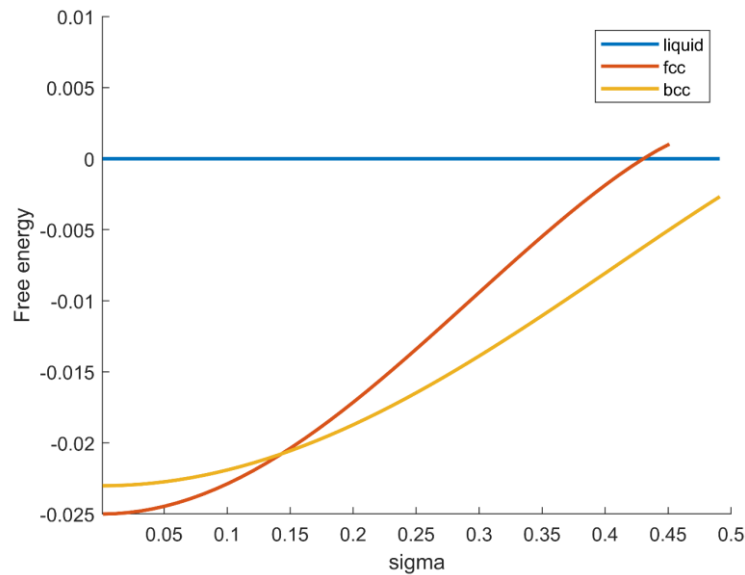


Fig. S1. The free energy of FCC and BCC phases with respect to effective temperature σ .

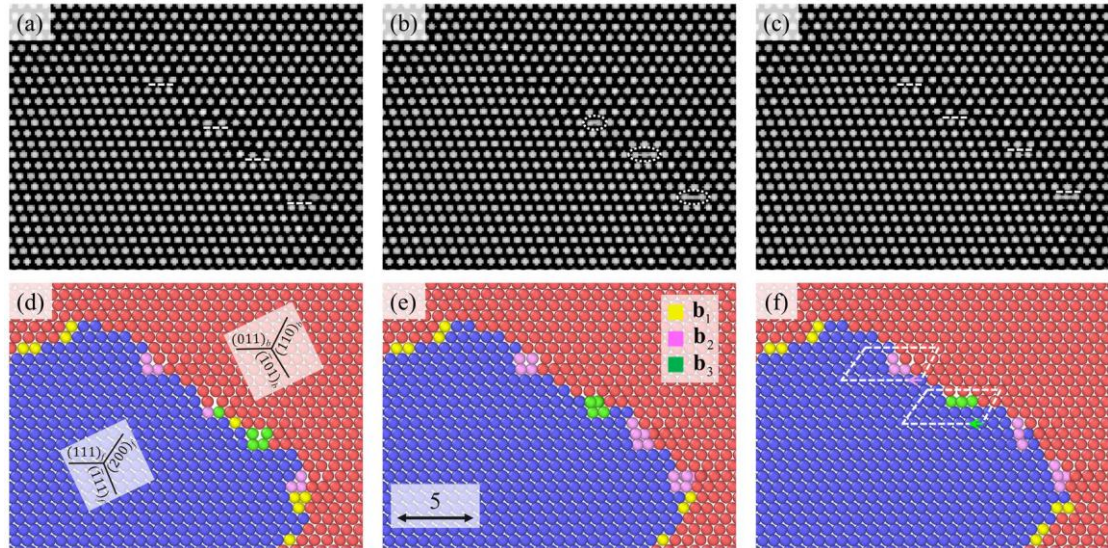


Fig. S2. Motion of the dislocation b_2 with climb components during the side facet migration process. **a–c** show the migration and non-conservative motion of three dislocations on the side facet, during which each dislocation moves upward by one atomic plane; the dashed lines indicate the slip planes at each dislocation core. **d–f** present the corresponding atomic configuration of the interface and the associated dislocation structures. The motion of the screw dislocation with Burgers vector b_1 is not visible in **a–c** due to projection effects.

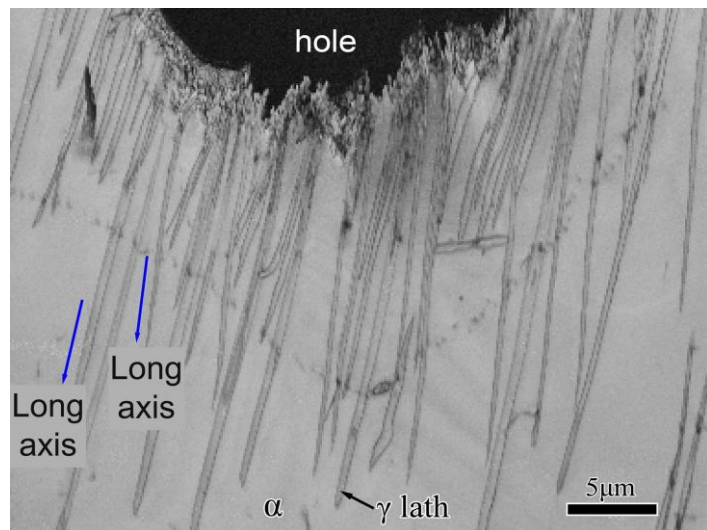


Fig. S3 Post-mortem overview of newly formed austenite laths after in situ TEM heating. EBSD band-contrast map acquired near the perforation edge of the electropolished foil after the in situ heating experiment, showing newly formed austenite laths embedded in ferrite matrix. Blue arrows indicate representative long axis directions, revealing that the lath long axes are predominantly aligned within the foil plane.

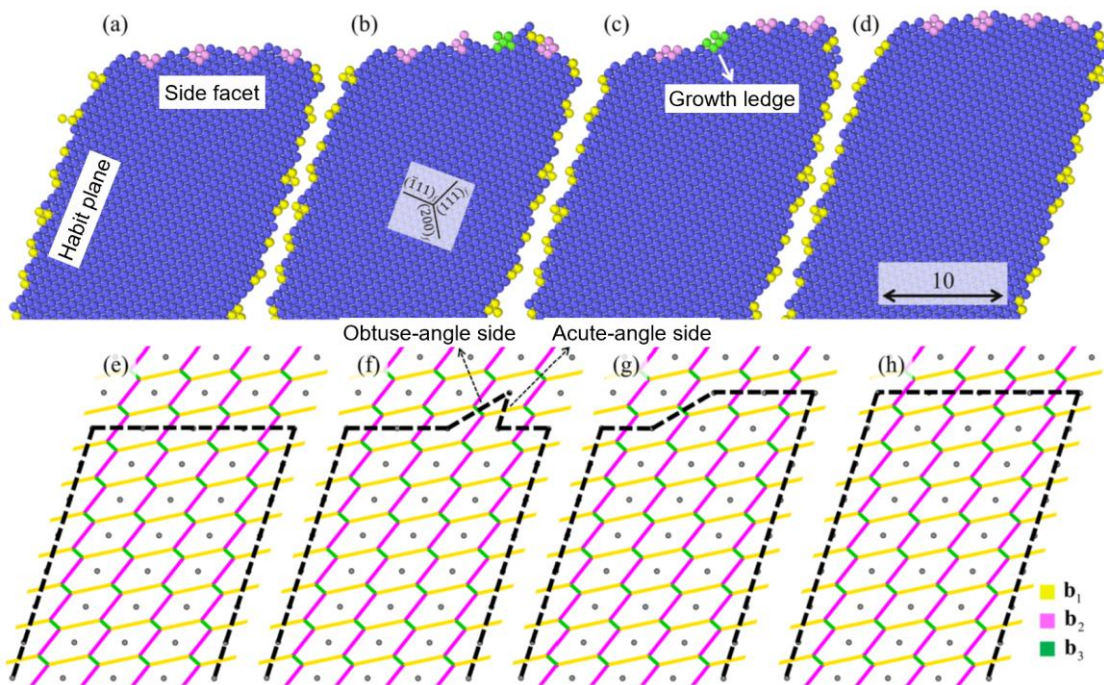


Fig S4. Cross-sectional views of the nucleation and propagation of a growth ledge on the side facet. Cross-sections taken on a plane perpendicular to the invariant line. **a–d** PFC snapshots; **e–h** corresponding O-lattice constructions. Grey dots denote edge-on O-lines; coloured segments denote O-cell walls associated with different Burgers vectors. Dashed lines are interface/ledge traces.

Table S1 Crystallographic features of PFC-predicted lath precipitate and experimentally observed lath precipitates across various alloys

	PFC	Duplex stainless steel ⁵	Cu-Cr alloys ^{22, 29}	Ni-Cr alloys ²⁸
OR	a_f/a_b	1.225	1.255	1.264
	$\theta_{p-p}(\circ)$	0	0.45	0
	$\theta_{d-d}(\circ)$	0	0.45	≤ 0.9
Long axis	$[0\bar{1}1]_f$	$[0.08 \bar{0.77} 0.64]_f$	$[0.13 \bar{0.76} 0.64]_f$	$[0.06 \bar{0.76} 0.65]_f$
HP	n _{HP}	$(2 \ 0.8 \ 0.8)_f$	$(2 \ 1.1 \ 1)_f$	$(2 \ 1.3 \ 1.1)_f$
	b _{HP}	b ₁	b ₁ [*]	-
	d_{HP}/a_f	2.4	2.5 [*]	-
SF	n _{SF}	$(\bar{1.1} \ 2 \ 2)_f$	$(\bar{0.4} \ 1.6 \ 2)_f$	$(\bar{0.7} \ 2 \ 2)_{f'}^{\sim}$ $(\bar{1.5} \ 2 \ 2)_{f'}^{\sim}$
	b _{SF-fine}	b ₂	b ₂ [*]	-
	$d_{SF-fine}/a_f$	3.3	3.3 [*]	3.4~4.1
	b _{SF-coarse}	-	$[110]_f/2[010]_b$	-
	$d_{SF-coarse}/a_f$	-	26.5	20.5~23.2
				32.9

θ_{p-p} : Angle between $(111)_f$ and $(011)_b$; θ_{d-d} : Angle between $[0\bar{1}1]_f$ and $[1\bar{1}1]_b$

OR: orientation relationship; HP: habit plane; SF: side facet;

n: facet normal; **b**: Burgers vector; *d*: dislocation spacing

* Calculated results based on geometric model